

Drought induces soil microbial stress responses and emissions of volatile organic compounds in an artificial tropical rainforest

Linnea Honeker (✉ linneah@email.arizona.edu)

University of Arizona <https://orcid.org/0000-0002-1299-0879>

Giovanni Pugliese

Max Planck Institute for Chemistry <https://orcid.org/0000-0002-2869-3588>

Johannes Ingrisch

University of Freiburg

Jane Fudyma

University of Arizona

Juliana Gil-Loaiza

University of Arizona

Elizabeth Carpenter

Lawrence Berkeley National Lab

Esther Singer

Lawrence Berkeley National Lab

Gina Hildebrand

University of Arizona

Lingling Shi

University of Göttingen

David Hoyt

Environmental Molecular Sciences Laboratory <https://orcid.org/0000-0002-2857-719X>

Jordan Krechmer

Aerodyne

Megan Clafin

Aerodyne

Christian Ayala-Ortiz

University of Arizona <https://orcid.org/0000-0001-8154-2378>

Viviana Freire-Zapata

University of Arizona <https://orcid.org/0000-0002-6306-1711>

Eva Pfannerstill

Max Planck Institute for Chemistry <https://orcid.org/0000-0001-7715-1200>

L. Daber

University of Freiburg

Michaela Dippold

University of Goettingen

Jürgen Kreuzwieser

University of Freiburg

Jonathan Williams

Max Planck Institute for Chemistry

S. Ladd

University of Basel <https://orcid.org/0000-0002-0132-5785>

Christiane Werner

University of Freiburg

Malak Tfaily

University of Arizona

Laura Meredith

University of Arizona

Article

Keywords: metatranscriptomics, microbial VOC, drought, soil microbial ecology, carbon, stable isotope, tropical rainforest

Posted Date: July 18th, 2022

DOI: <https://doi.org/10.21203/rs.3.rs-1840246/v1>

License:   This work is licensed under a Creative Commons Attribution 4.0 International License.

[Read Full License](#)

Version of Record: A version of this preprint was published at Nature Microbiology on July 31st, 2023. See the published version at <https://doi.org/10.1038/s41564-023-01432-9>.

Abstract

Drought impacts microbial carbon cycling, and thus the fate of carbon in soils. Carbon allocation to energy via CO₂ producing respiration and to biosynthesis via volatile organic compound (VOC) emissions both represent consequent carbon loss to the atmosphere, although only the former is well studied. Here, we examined drought impacts on carbon allocation by soil microbes to CO₂ and VOCs using position-specific ¹³C-labeled pyruvate and multi-omics in an artificial tropical rainforest. During drought, ¹³C-VOCs efflux increased, driven by increased production and buildup of intermediate metabolites due to decreased interconnectivity between central carbon metabolism pathways, and ¹³C-CO₂ efflux decreased, driven by an overall decrease in microbial activity. However, internal carbon allocation to energy relative to biosynthesis did not change, signifying maintained energy demand toward biosynthesis of VOCs and drought-stress induced biosynthesis pathways. Therefore, while carbon loss to the atmosphere via CO₂ decreases during drought, carbon loss via VOCs may increase.

1. Main

Microorganisms regulate terrestrial carbon (C) cycling in fundamental ways¹, including transforming soil C into gaseous compounds that can escape to the atmosphere, primarily as CO₂ through microbial heterotrophic respiration. However, microbes also produce volatile organic compounds (VOCs) as metabolic intermediates, signaling molecules, and secondary metabolites^{2,3}. In fact, volatile metabolites represent an often overlooked subset of the complete soil metabolome^{4,5}, and their emissions to the atmosphere not only represent soil C loss, but contribute to atmospheric chemistry including ozone formation and cloud condensation nuclei⁶. Therefore, characterizing microbe-mediated C flow along the soil-atmosphere continuum is critical for understanding the fate of soil C and VOC emissions to the atmosphere under projected environmental changes, including drought.

Drought stress induces well-characterized microbial physiological responses that impact C metabolism, such as biosynthesis of protective molecules (e.g., osmolytes and extracellular polymeric substances) to preserve cell integrity^{7,8}, retain moisture, and concentrate resources^{9,10}. Production of these biomolecules is energy intensive, and may divert resources from biomass synthesis⁹, leading to decreased growth-fueling heterotrophic respiration and CO₂ emissions^{11,12}. Drought also induces changes in soil C composition and availability¹³⁻¹⁵, further impacting microbial activity^{16,17}, e.g., by inducing shifts in substrate utilization¹⁸. Overall, it remains unclear how drought-induced shifts on microbial metabolism and soil C composition influence C allocation to volatile metabolites, which can mitigate drought stress in plants¹⁹. Moreover, soil water content may have a strong impact on VOC emissions from tropical soils^{20,21}, perhaps driven by drought impacts on microbial VOC biosynthesis. Characterizing changes in microbial C cycling and allocation is particularly important in tropical rainforest soils where droughts will likely occur more frequently and last longer due to climate change^{22,23}.

Detecting shifts in microbial C cycling and allocation within complex metabolic networks encompassing competing production and consumption pathways is difficult. This complexity can be addressed by tracking microbe-mediated C flow through soils using isotopically labeled central metabolites. Position-specific ^{13}C -glucose and/or ^{13}C -pyruvate labeling has been used to track microbial C allocation to CO_2 and biomass in soil mesocosms^{24–26}, however, studies on drought in the field and allocation to VOCs are missing²⁷. The direct metabolic information derived from isotope labeling can be contextualized using powerful, information-rich constraints provided by ‘omics approaches that profile the gene content, gene expression, and metabolomes of soil microbiomes⁵. Together, these approaches can uncover metabolic drivers of shifting microbial C cycling and allocation in soils under drought.

In this study, we performed a comprehensive assessment of how drought impacts soil microbial C allocation to CO_2 and VOCs in an enclosed tropical rain forest using an integrated approach, combining position-specific ^{13}C -pyruvate-labeling with metatranscriptomics, metagenomics, and metabolomics. With the assumption that the C1 position of pyruvate would enter CO_2 via decarboxylation during biosynthesis or respiration (tricarboxylic acid [TCA] cycle), and the C2 position would enter VOCs (as biosynthesis) or CO_2 during respiration, we could infer microbial C allocation to biosynthesis vs. TCA cycle. We hypothesized that during drought: 1) microbial C allocation to the TCA cycle would decrease as C allocation is diverted to increased biosynthesis of stress compounds, including VOCs, and 2) changes in C allocation would be associated with shifts in metabolic composition and gene expression.

2. Results And Discussion

2.1 Gaseous emissions from soil

We tracked ^{13}C from the 1st and 2nd positions of pyruvate ($^{13}\text{C1}$ -pyruvate and $^{13}\text{C2}$ -pyruvate, respectively) into CO_2 and VOCs (Fig. 1). During drought, both the overall soil CO_2 efflux and its ^{13}C enrichment ($\delta^{13}\text{C}_{\text{CO}_2}$) after injection of $^{13}\text{C1}$ -pyruvate and $^{13}\text{C2}$ -pyruvate decreased relative to pre-drought ($p < 0.001$ for mean fluxes) (Fig. 2a; **Fig S1a**). As expected, the efflux of CO_2 released from $^{13}\text{C1}$ -pyruvate had a higher $\delta^{13}\text{C}$ value compared to $^{13}\text{C2}$ -pyruvate injection during both pre-drought and drought ($p < 0.001$ for mean value; Fig. 2a), and this pattern was reflected in the cumulative ^{13}C - CO_2 effluxes (Fig. 2b).

Microbes maintained their allocation to energy production during drought-induced stress. This was because while overall C allocation to biosynthesis was higher during pre-drought conditions (Fig. 2c), internal partitioning of C to biosynthesis vs TCA cycle did not change (**Fig S1b**), contrary to our hypothesis.

To further reveal C allocation strategies, we tracked ^{13}C from pyruvate into volatile metabolites. Drought induced an increased efflux of ^{13}C -enriched central volatile metabolites (acetone, acetic acid, and $\text{C}_4\text{H}_6\text{O}_2$) after $^{13}\text{C2}$ -pyruvate injection (Fig. 2d-f), indicating synthesis along metabolic pathways after C1

decarboxylation to CO₂. Cumulative effluxes of ¹³C-acetic acid, ¹³C-acetone, and ¹³C-C₄H₆O₂ from chambers receiving ¹³C2-pyruvate increased significantly during drought ($p \leq 0.05$; Fig. 2g-i). Acetic acid was the only VOC that had a ¹³C-enriched continuous efflux (Fig. 2e) and significantly increased cumulative efflux ($p < 0.01$; Fig. 2g) during drought from chambers that received ¹³C1-pyruvate, and a negative cumulative efflux from both labels during pre-drought, indicating acetate consumption (Fig. 2e). ¹³C-enrichment of acetic acid indicates active acetogenesis, where acetogens fix two CO₂, in this case ¹³C-CO₂, and four H₂ molecules to form acetyl-CoA, which is further reduced to acetate (Fig. 1)²⁸, an intermediate of central metabolism which can be protonated in soils and volatilized as acetic acid (hereafter referred to as acetate). C₄H₆O₂ could be diacetyl and/or one other unidentifiable compound based on structural identification of compounds with this formula from nearby locations (**Fig S2**). ¹³C may have been allocated to other non-volatile metabolites, however no such ¹³C-enrichment was detected by 1H- NMR.

Drought induced a major readjustment of overall C allocation. The proportion of ¹³C from pyruvate allocated to biosynthesis dropped from 41.5 to 17.5% and to the TCA cycle dropped from 21.3 to 11.2% during drought (Fig. 2j). Meanwhile, unaccounted for ¹³C ('other'), representing unmetabolized pyruvate or other uncharacterized pathways, increased from 37.2 to 71.3%. The proportion of biosynthesis devoted to VOCs increased substantially during drought, from < 2 to almost 60% of biosynthetic products. Together, these data suggest that microbes shift from preferential biosynthesis of other non-volatile compounds and/or biomass during pre-drought to protective biomolecules⁸ including VOCs during drought, supporting our hypothesis. A majority of biosynthesis went towards acetone; emissions of acetone also increased during low moisture in a previous study in the tropical rainforest²⁰, supporting a microbial role in acetone biosynthesis and a potential role in drought-tolerance.

2.2 Acetate, acetone, and diacetyl cycling gene expression

To further characterize active metabolic pathways that could cycle acetate, acetone, and diacetyl, we examined soil microbial gene expression, using metatranscriptomics and metagenomics from a gene-centric approach to identify: 1) specific genes that may be driving the ¹³C-enriched VOC emissions and 2) overall gene expression patterns that would portray ecosystem-scale microbial activity. Drought and pyruvate addition impacted overall gene expression profiles ($p < 0.05$) (**Fig S3a**) and taxonomic composition of active microbial communities (**Fig. S3b,c**), while only location (site) impacted microbial functional potential ($p < 0.05$) (**Fig S3c**), with no impact on taxonomic composition (**Fig S3d,e**). This demonstrates that fluctuating gene expression was driven by changes in microbial activity and not drastic shifts in community composition.

Acetate is a central metabolite that can be rapidly cycled by microbes via several pathways downstream of pyruvate (Fig. 3a). Expression of genes encoding acetate-producing enzymes increased during drought (Fig. 3b), perhaps driving increased acetate buildup in the soil and emission to the atmosphere as acetic

acid. The most upregulated genes were *poxB* (K00156; PDH-quinone) and *poxL* (K00158; pyruvate oxidase), particularly at 0 and 6 h post pyruvate injection ($p < 0.05$) (Fig. 3b; **Fig S4xx**), which were also positively correlated with the efflux of ^{13}C enriched acetate from $^{13}\text{C}_2$ -pyruvate (hereafter referred to as acetate-C2) ($\rho = 0.40$ and 0.41 , respectively, $p < 0.05$; Table 1). The *poxB* gene, first identified in *Escherichia coli*^{29,30}, encodes for the protein PDH-quinone, which catalyzes the direct conversion of pyruvate to acetate and CO_2 via oxidative decarboxylation, with quinone or menaquinone as the electron acceptor^{29,30}. Quinone then shuttles the electrons to the electron transport chain where O_2 is the final electron acceptor, thereby producing ATP³¹. The strong upregulation of *poxB* during drought suggests that this gene may improve microbial fitness during drought, perhaps to gain extra energy for biomolecule production, as discussed below.

Another gene encoding an acetate-cycling enzyme upregulated during drought was *ACH1* (K01067), particularly before pyruvate injection at 0 h ($p < 0.001$) (Fig. 3b; **Fig S4x**). *ACH1* was also positively correlated with acetate-C2 efflux ($\rho = 0.59$; $p < 0.01$) (Table 1), perhaps due to its direct role in acetate production, or consumption if increased acetate concentrations stimulate its activity. While genes encoding for other acetyl-CoA hydrolases are present in bacteria³², *ACH1* is only present in the mitochondria³³ of eukaryotes, including fungi^{34,35}. *ACH1* encodes for a gene with sequence similarity to either an acetyl-CoA hydrolase, which can produce acetate and CoA^{35,36} and may play a role in transporting acetate from acetyl-CoA across organelle membrane to cytosol for conversion back to acetyl-CoA^{35,36} by acetyl-CoA synthetase (*acs*; K01895), or a CoA-transferase which can transfer CoA from succinyl-CoA to acetate, thus consuming acetate and playing a role in acetate detoxification³⁴. As a central node in metabolism, acetyl-CoA intersects multiple metabolic pathways and can directly feed into the TCA cycle (in mitochondria for eukaryotes) or serve as a precursor for fatty acids and isoprenoid production (in cytosol for eukaryotes)³⁷. In this study, while the *acs* gene was uniformly expressed across all time points (Fig. 3b; **Fig S5a**), it was negatively correlated with acetate-C2 efflux ($\rho = -0.40$, $p < 0.05$) (Table 1), indicating it may have indeed played a role in acetate consumption. Unlike *ACH1*, *acs* is present in archaea and bacteria too and plays a role in methanogenesis³⁸, therefore, potential *acs* downregulation in archaea/bacteria during pre-drought may have offset any *acs* upregulation in fungi during drought.

During drought, expression of genes encoding acetone-consuming enzymes were downregulated while that of acetone-producing enzymes remained consistent (Fig. 3b), leading to an overall increase in acetone buildup in the soil and emissions to the atmosphere. Acetone is produced via acetoacetate decarboxylase, encoded for by the gene *adc* (K01547), which had a slightly positive, but not significant, correlation with acetone-C2 ($\rho = 0.30$, $p = 0.08$) and no significant change with drought compared to pre-drought at any time point (Fig. 3b). However, there was an increase in *adc* expression at 48 h post pyruvate addition compared to 0 h during drought ($p < 0.05$) (**Fig S5b**), which could have contributed to increased ^{13}C -enriched acetone emissions. The gene *adc* is part of the acetone-butanol-ethanol (ABE)

fermentation pathways in *Clostridium acetybuticum* and related species^{39,40}, however, we did not see expected concurrent ¹³C-enriched ethanol or butanol emissions.

Several possible acetone-consuming reactions decreased during drought. First, acetone conversion to methyl acetate via acetone monooxygenase, encoded by *acmA* (K18371), was strongly downregulated during drought (at 0 h, $p < 0.01$) (Fig. 3b) and negatively correlated with acetone-C2 ($\rho = -0.36$, $p < 0.05$) (Table 1). While $C_3H_6O_2$ was detected, possibly indicating methyl acetate, there was no efflux of ¹³C-enriched $C_3H_6O_2$. However, methyl acetate can break down to methanol and ¹³C-acetate, which could have been further consumed during pre-drought conditions, as explained above (i.e., methanogenesis) (Fig. 3a). Another possible acetone consumption pathway is conversion to 2-propanol via alcohol dehydrogenase, encoded by the gene *adh1* (K18382), which was positively correlated with acetone-C2 efflux ($\rho = 0.45$, $p = 0.05$). However, 2-propanol was not detectable due to its extreme fragmentation during ionization with PTR-MS⁴¹. Another acetone consuming reaction occurs via acetone carboxylase, encoded for by the genes *acxA*, *acxB*, and *acxC* (K10855, K10854, and K10586), which converts acetone to acetoacetate (Fig. 3a). Genes for all three acetone carboxylase subunits were downregulated during drought ($p < 0.05$) (Fig. 3b). Therefore, the significant decrease in acetone consumption during drought conditions drove the increase in ¹³C-enriched acetone emissions, signifying that changes in VOC fluxes from soils depend not just on production, but also internal consumption.

Diacetyl production can occur immediately downstream of pyruvate within the butanoate metabolism pathway where K01652 (*ilvB*), which encodes for acetolactate synthase (large subunit), catalyzes the conversion of pyruvate to acetolactate and CO_2 (Fig. 3a). However, during drought, *ilvB* was downregulated ($p < 0.05$) (Fig. 3b), and therefore does not match the increase in ¹³C-enriched $C_4H_6O_2$ emissions. The unidentified $C_4H_6O_2$ compound, which could have been succinic aldehyde, methyl acrylate, or 2-butenate, may have also driven ¹³C-enriched emissions, though none of these are part of KEGG pathways, making it difficult to assess genes involved in cycling of $C_4H_6O_2$.

Table 1

Correlations between ^{13}C -enriched VOCs (acetate, acetone, and diacetyl) after labeling with $^{13}\text{C}_2$ -pyruvate and expression of genes known to cycle these compounds. Spearman correlation coefficients (ρ) were calculated between gene expression (normalized gene copies) and ^{13}C -enriched VOCs.

Cycling of:	Gene name	KO	Enzyme	Correlation Coefficient (ρ)		
				Acetate	Acetone	Diacetyl
Acetate	<i>ACH1</i>	K01067	acetyl-CoA hydrolase	0.59**	0.53**	0.19
	<i>poxB</i>	K00156	PDH-quinone	0.40*	0.41	-0.16
	<i>poxL</i>	K00158	pyruvate oxidase	0.41*	0.40	-0.15
	<i>ackA</i>	K00925	acetate kinase	-0.11	-0.28	0.37
	<i>acyP</i>	K01512	acylphosphatase	-0.31	-0.28	-0.05
	<i>pct</i>	K01026	propionate CoA-transferase	-0.28	-0.25	0.36
	<i>acs</i>	K01895	acetyl-CoA synthetase	-0.40*	-0.37	-0.05
	<i>aarC</i>	K18118	succinyl-CoA:acetate CoA-transferase	0.40*	0.59*	0.53*
Acetone	<i>adh1</i>	K18382	NAD ⁺ -dependent secondary alcohol dehydrogenase	0.07	0.34	-0.10
	<i>adc</i>	K01574	acetoacetate decarboxylase	0.18	0.30	0.27
	<i>acxA</i>	K10855	acetone carboxylase, β -subunit	-0.28	-0.23	0.08
	<i>acxB</i>	K10854	acetone carboxylase, α -subunit	-0.21	-0.19	0.17
	<i>acxC</i>	K10856	acetone carboxylase, γ -subunit	-0.38*	-0.49*	-0.06
	<i>acmA</i>	K18371	acetone monooxygenase	-0.51**	-0.36	0.12
Diacetyl	<i>BDH</i>	K00004	butanediol dehydrogenase	0.15	0.04	0.15
	<i>ilvB</i>	K01652	acetolactate synthase, large subunit	-0.50*	-0.57**	-0.03
	<i>butA</i>	K03366	meso-butanediol dehydrogenase	0.02	0.09	0.17

*, $p < 0.05$; **, $p < 0.01$ (FDR-corrected); KO, KEGG orthology; VOC, volatile organic compound; PDH, pyruvate dehydrogenase

2.3 Multi-omics: Metabolomics, substrate composition, and microbial gene expression

To place ^{13}C -enriched emissions of acetate, acetone, and diacetyl and the metabolic pathways involved in the cycling of these volatile metabolites into the context of overall microbial activity and substrate availability, we further characterized soil metabolites and microbial gene expression.

Metabolite composition shifted between pre-drought and drought conditions, which separated along the first component (PC1), explaining 44.7 and 62.3% of variation in small (< 200–300 Da) compounds measured using ¹H-NMR (Fig. 4a) and relatively larger compounds (> 200 Da) characterized using FTICR-MS (Fig. 4b), respectively. Small compounds, mainly representing primary metabolites, that decreased during drought included several amino and keto acids, while only trehalose, a common osmolyte produced by bacteria during times of water stress⁴², increased during drought ($p < 0.05$) (**Table S1**). Drought can induce increased soil concentrations of trehalose^{14,15}, yet the impact on amino acids is variable^{14,15,43}. While we did not detect non-volatile ¹³C-enriched primary metabolites with ¹H-NMR, decreased concentrations of amino acids during drought could indicate decreased C allocation to biosynthesis of biomass or enhanced degradation of proteins.

For relatively larger compounds, representing microbial metabolism and substrate availability, recalcitrant lignin-, condensed hydrocarbon-, and tannin-like compounds increased and bioavailable protein- and carbohydrate-, along with lipid-like compounds, decreased during drought (Fig. 4b, **Fig S6**). These findings contrast with previous observations of decreased lignin and increased amino-acid content during drought in a tropical rainforest¹⁵. However, these past experiments did not have the increased control of moisture and significant decrease in soil moisture (26.0 ± 6.9 to $13.8 \pm 2.6\%$; $p < 0.001$) we achieved in our enclosed experiment. Our results indicate that microbes consumed most bioavailable compounds during drought, with a concurrent decrease in labile C replenishment from plant root exudation⁴⁴. Furthermore, plant production of lignin-like compounds may have increased during drought, for example, by *Piper* sp.⁴⁵.

Next, we looked at overall shifts in microbial metabolic pathways of co-expressed gene modules using WGCNA. We identified a total of nine modules, four of which were associated with condition (pre-drought or drought) and acetate-C2 and acetone-C2 effluxes (**Fig. S7**).

The pre-drought associated brown module was enriched in C cycling pathways. The association of the brown module with pre-drought conditions was demonstrated by its negative correlation with ($r = -0.6$; $p < 0.001$) (**Fig S7b**) and downregulation during ($p < 0.001$) (Fig. 5a) drought. The enriched central C metabolic pathways interwoven within the brown module included C metabolism, butanoate metabolism (includes acetone and diacetyl cycling), and pyruvate and methane metabolism (both include acetate cycling) (Fig. 5a). In fact, methanogenesis, part of the methane metabolism pathway, can act as a 'scavenger' of fermentation products, including acetate⁴⁶, supported by its negative correlations with acetate-C2 and acetone-C2 efflux ($r = -0.43$ and -0.46 , respectively; $p < 0.05$) (**Fig S7b**). Therefore, efficient C cycling in the brown module led to rapid consumption of metabolic intermediates preventing losses to the atmosphere under moist, anoxic conditions.

The drought-associated pink module played a role in osmotic stress adaptation, quinone production, and acetate biosynthesis. The pink module was positively correlated with ($r = 0.8$; $p < 0.001$) (**Fig S7b**) and upregulated during ($p < 0.05$) (Fig. 5b) drought, and it was also involved in acetate production, indicated by its positive correlation with acetate-C2 ($r = 0.4$; $p < 0.05$) (**Fig S7b**) and inclusion of the acetate-producing *poxB* and *poxL* genes. Furthermore, the pink module was enriched in starch and sucrose

metabolism; alanine, aspartate, and glutamine metabolism; and ribosome pathways (Fig. 5d). Biosynthesis of trehalose within the starch and sucrose metabolism pathway corresponds to the increase in trehalose concentrations observed during drought (Sec 2.3.1). At the sub-pathway level, biosynthesis of ubiquinone, a type of quinone, was also enriched, indicating a possible association with osmotic stress. We hypothesize two explanations that connect quinone biosynthesis, *poxB* expression, and acetate biosynthesis as stress-response mechanisms during drought. First, a link between the electron transport chain and osmotic regulation is possible. As an immediate microbial response to osmotic stress, microbes actively influx K⁺, which then promotes trehalose biosynthesis⁴⁷. A supercomplex of H⁺-ATPase and K⁺ pumps may form in the cellular membrane as part of the electron transport chain⁴⁸. Therefore, increased production of quinone and transport of electrons to the electron transport chain could be linked with K⁺ influx, leading to further osmotic adjustment. Second, due to the high demand for protective biomolecule synthesis (i.e., trehalose), there is a high demand for energy production during drought, which may be limited by lower TCA cycle activity (Fig. 2j). To address this need, *poxB* may act as a bacterial PDH bypass route for production of acetyl-CoA (in combination with *acs*)⁴⁹, the precursor to many downstream secondary metabolites⁵⁰ (Fig. 3a). While experiments in *Corynebacterium* found that the PDH bypass route was not essential for growth³⁰, *poxB* contributes to the aerobic growth efficiency in glucose-limited conditions in *E. coli*⁴⁹. It is, therefore, possible that under times of stress or within different bacterial species, this route improves fitness by increasing acetyl-CoA production to meet energy demands. Notably, the decreased C cycling efficiency during drought could also be driven by increased soil porosity and decreased flow of metabolites (volatile and non-volatile), thereby isolating microbial communities and their products to micro-niches within the soil medium¹².

The drought-associated green and magenta modules were enriched in fungal and archaeal metabolic pathways, respectively. Both modules were significantly correlated with ($r = 0.54$ and 0.36 , respectively; $p < 0.05$) (**Fig S7b**) and upregulated during ($p < 0.05$) (Fig. 5c,d) drought, however while the green module was positively correlated with acetate-C2 and acetone-C2 ($r = 0.77$ and 0.76 , respectively; $p < 0.001$) (**Fig S7b**) and contained the acetate-cycling genes *ACH1* and *adc*, the magenta module showed no correlation with VOC emissions or genes of interest. The green module was enriched in ribosome, including pathways that are ubiquitous across all organisms, and oxidative phosphorylation, including fungi-specific enzymes (NADH:ubiquinone oxidoreductase and F-type ATPase) (Fig. 5c) (KEGG pathway database; [/www.genome.jp/kegg/pathway.html](http://www.genome.jp/kegg/pathway.html)). Together, this indicates that this module enriched in fungal genes played a role in compound biosynthesis during drought, perhaps to assist in drought tolerance (i.e. osmolytes, other secondary metabolites, etc). While we did not see a significant increase in active fungi during drought based on taxonomic classification (**Fig S3**), fungi may nevertheless have shifted their activity during drought as a stress-response. In fact, drought tends to induce increased abundance of fungi compared to bacteria and fungal communities are generally more resistant to stress than bacteria^{51–53}. Furthermore, the association between the green module and acetate cycling suggests a potential role of fungi in acetate and acetone fermentation. Specific studies examining fungal

production of acetone are very limited, however, acetone production by *Penicillium brevicompactum* has been detected⁵⁴.

In contrast, the magenta module was enriched in pathways specific to archaea. For instance, the oxidative phosphorylation pathway was also enriched in the magenta module (Fig. 5d), but specifically with archaeal-specific enzymes including a V/A-type ATPase. Similarly, within the RNA polymerase pathway that was enriched in the magenta module (Fig. 5d), almost all genes are specific to archaeal RNA polymerases. This presence of an archaeal-dominated module during drought corresponds to increased active archaeal abundance, specifically thaumarchaeota (**Fig S4b,c**). Collectively, these results suggest that microbial acetate and acetone biosynthesis during drought may be associated with fungal rather than archaeal metabolic activity, a finding not previously reported.

2.4. Conclusion

In an enclosed tropical rainforest, microbially-mediated gaseous efflux shifted during drought; ¹³C-CO₂ emissions decreased and ¹³C-enriched VOCs (acetate, acetone, and diacetyl) emissions increased. Despite the increase in emissions of these volatile metabolites, ecosystem-wide C allocation to microbial biosynthesis decreased during drought, reflecting an increase in proportion of biosynthetic products that were volatile (Fig. 2j). While we cannot definitively state where C was allocated besides CO₂ and VOCs, we hypothesize that during pre-drought conditions, C allocation to biosynthesis was directed towards biomass⁹. During drought, internal C allocation to biosynthesis vs. TCA cycle remained constant, indicating that maintaining energy production is necessary to meet the demands of drought-induced stress pathways, such as biosynthesis of trehalose and quinone. Further probing of multi-omics, specifically metatranscriptomics and metabolomics, provided further context for these emission patterns. During pre-drought acetate and acetone consumption was higher, indicating increased C cycling efficiency without volatile escape to the atmosphere, however during drought, this C cycling efficiency decreased as substrates became less bioavailable and microbes shifted their energy to drought-stress pathways. This suggests that soil emissions of 'leaky' central C metabolites such as acetate and acetone may play an active role in microbial survival during drought, perhaps through communication with other organisms, as could-generating condensation nuclei⁵⁵, and even a direct impact on nutrient availability⁵⁶. Moreover, these results demonstrate a shifting dynamic of soil C loss which has been previously overlooked. While changes in microbial activity and C cycling drive a decrease in microbially-mediated C loss to the atmosphere in the form of CO₂, there is an ecosystem-wide increase in C allocation to volatile intermediate metabolites, therefore, maintaining soil C loss with an impact on global C budgets and be a potential feedbacks to climate change⁵⁷.

3. Methods

3.1 Biosphere 2 tropical rainforest description and drought experiment

Biosphere 2 (B2) in Oracle, AZ is a 1.27 ha steel and glass-enclosed building harboring five distinct biomes, including a 0.19 ha tropical rainforest (TRF), an enclosed ecosystem with variable topography and microhabitats with the ability to control rain and temperature inside providing an optimal setting for studying drought effects^{58–60}. The B2 TRF harbors approximately 70 species of trees and shrubs, forming a canopy and understory, with soils that represent biogeochemical cycles present in rainforests⁶¹. In late 2019, a 65-day drought experiment was conducted as part of the Water, Atmosphere, and Life Dynamics campaign (WALD)⁴⁴. During ambient (pre-drought) conditions, rainfall events were simulated by spraying 15,000 L of irrigation water from the top of the B2 TRF at a frequency of 3 days a week. The last rainfall event before the drought was on October 7, 2019, and the first post-drought rainfall was on December 12, 2019. During the drought, ambient temperatures were maintained in the lowland region between 20 to 26.7 °C. For more detailed characterization of the WALD drought experiment, please refer to ⁴⁴.

3.2 Position-specific (C1 and C2) ¹³C pyruvate labeling

Soil was labeled with position-specific (C1 or C2) ¹³C-pyruvate (henceforth referred to as C1-¹³C-pyruvate and C2-¹³C-pyruvate, respectively) to track C allocation into CO₂, VOCs, and primary metabolites, as done previously in plants^{45,62}. Three replicates each of C1-¹³C-pyruvate or C2-¹³C-pyruvate labeling was performed per site in the B2 TRF (Site 1, Site 2, and Site 3; n = 6 per site) (**Fig S1a**) within soil chambers (**Fig S1b**). ¹³C labeling was performed before and during drought (September 12 - 15 and November 7-19, respectively). The night before labeling, two automatic chambers were placed onto the corresponding soil collars and covered with a rain-out shelter. Each morning, these collars were labeled at around 10AM by using a 5x5 cm stencil with 1x1 cm openings placed into one side of each chamber and adding 100 µl of C1-¹³C-pyruvate or C2-¹³C-pyruvate solution (40 mg/ml) to each opening to a depth of 1 cm, for a total of 25 injections (**Fig S1b**). The stencil was then removed prior to soil chamber gas measurements.

Soil moisture and temperature was measured using a portable probe and LabQuest viewer (Vernier, Beaverton, OR, USA). For pre-drought, soil moisture and temperature data were collected on October 1 and 9 and for drought on November 11 and 18 for a subset of collars (P11, P21, P23, P32, and P33 [Site #, replicate #]), except for November 18, where all collars from the experiment were tested (see **Fig S1a**). Soil moisture measured near the labeling sites decreased from 26.0 ± 6.9 to 13.8 ± 2.6 % (p < 0.001) between pre-drought and drought conditions, respectively. Soil temperature did not change significantly, and ranged from 23.0 ± 0.6 during pre-drought and 23.3 ± 1.2 °C during drought.

3.3 Continuous monitoring of VOCs and CO₂

Prior to labeling, collars were measured at typical temporal resolution (~ 2 hr) over night. In order to capture any rapid changes in gas fluxes due to changes in microbial activity after pyruvate addition, measurement intervals were increased to high frequency (30 minutes) directly prior to labeling. After gas fluxes were expected to equilibrate, approximately 8 hr post pyruvate labeling (~ 6 PM), measurement intervals were decreased to low frequency (50 minutes) and remained at this frequency until measurements were stopped at 48 hr post labeling. For each measurement, the automatic chamber closed over the collar for a total of 10 min (pre-purge, 2.5 min; measurements, 6.5 min; post-purge, 1 min). Fluxes were measured using an automated, multiplexed Licor soil flux system (Licor 8100, Li-8150 16-port multiplexer and Lic 8100-104 Long-Term Chambers with opaque lids, Licor Inc.). The system was coupled to a Picarro G2201-i analyzer (Picarro Inc., Santa Clara, US) to measure CO₂ and isotopic composition and a proton-transfer-reaction time-of-flight mass spectrometer (PTR-TOF 8000, Ionicon Inc. Innsbruck, Austria) for VOCs (including ¹³C-VOCs). The PTR-ToF-MS sampled the sub-flow from the soil flux system at 30 sccm *via* fluorinated ethylene propylene tubing heated at 60 °C. The drift voltage was 600 V, the drift temperature was 60°C and the drift pressure was 2.2 mbar, resulting in an E/N ratio of 137 Td. The time resolution was 10 ms and the mass range was up to 500 amu. The PTR-ToF was operated in the H₃O⁺ mode, therefore only compounds having proton affinity higher than water (697 kJ/mol) underwent proton-transfer reactions and could be detected on their protonated mass to charge ratio (*m/z*), which includes the vast majority of VOCs. Measured ions were attributed to chemical formulas and specific chemical species based on the exact protonated *m/z*. PTR-TOF data were processed using the software PTRwid⁶³. To account for possible variations of the reagent ion signals, measured ion intensities were normalized to the H₃O⁺ counts in combination with the water-cluster ion counts⁶⁴. At midnight, automatic calibrations were performed using standard gas cylinders containing different multi-VOC component calibration mixtures in Ultra-High Purity (UHP) nitrogen (Apel-Riemer Environmental, Inc., Colorado, USA). For a detailed description of the calibration setup see Werner et al. (2021). The concentrations of compounds included in the standard were calculated with an uncertainty of ≤23%. Concentrations of compounds not included in the calibration standard cylinders were calculated by applying the kinetic theory of proton transfer reaction^{65,66} with an uncertainty of ≤50%.

Select additional soil experiments were conducted with a Vocus proton transfer reaction time-of-flight mass spectrometer (PTR-TOF; TOFWERK, AG, Thun, Switzerland)⁶⁷ coupled to a custom-built gas chromatograph (GC; Aerodyne Research, Inc., Billerica, MA, USA)⁶⁸. The GC contains an integrated two-stage adsorbent-based thermal desorption preconcentration system for *in situ* collection of VOCs prior to separation on the chromatographic column. For preconcentration, a multi-bed (Tenax TA/Graphitized Carbon/Carboxen 1000; Markes International) sorbent tube was used for the first stage of sample collection, this tube is then subjected to a post-collection water purge before the sample was thermally desorbed to a multi-bed focusing trap (Tenax, Carbopack X, Carboxen 1003; Markes International) prior to injection onto the GC column. For this study, the GC was equipped with a 30-m Rxi-624 column (Restek, 0.25 mm ID, 1.4 µm film thickness) which resolves non- to mid-polarity VOCs in the C₅ - C₁₂ volatility range prior to ionization in the PTR detector. The GC-PTR sampled from *in-situ* soil gas probes⁶⁹ on an

alternating timed schedule. The GC-PTR can speciate structural isomers and help identify some unknowns by matching to calibrated retention times.

3.3.1 CO₂ data analysis

CO₂ fluxes and their isotopic composition were calculated based on data from the Picarro isotope analyzer. Fluxes were calculated with linear and exponential models, fitted to each individual chamber measurement. A deadband of 30 s was used for each measurement to allow for mixing in the chamber. The linear models were calculated based on the first 120 s, for the exponential model the full closure period of 6.5 min was used. Fluxes were quality controlled visually. Fluxes based on the exponential fit were used preferentially but replaced by the linear-fit flux where necessary. The isotopic composition was calculated based on the individual efflux rates of the ¹²C-CO₂ and ¹³C-CO₂ isotopologue. These are reported separately by the gas analyzer, and linear fits based on the first 120 s were used to calculate efflux rates. Due to the high enrichment of the labeled soil CO₂ efflux, this method was found to be more reliable compared to conventional Keeling-plot approaches. The isotopic composition of the CO₂ efflux was then calculated from the ratios of ¹²C-CO₂ and ¹³C-CO₂ efflux rates and normalized to the Vienna Pee Dee Belemnite (VPDB) scale ($\delta^{13}\text{C}_{\text{CO}_2} = ((^{13}\text{C}/^{12}\text{C})_{\text{CO}_2})/((^{13}\text{C}/^{12}\text{C})_{\text{VPDB}}) - 1$). C isotope fluxes were quality controlled visually for each individual chamber and outliers removed manually.

¹³C-CO₂ emitted from chambers that received ¹³C1-pyruvate is formed as C is decarboxylated via pyruvate dehydrogenase (PDH) to form acetyl-CoA or via an alternate decarboxylation reaction leading to biosynthesis of compounds (e.g., biomass, secondary metabolites, VOCs), while ¹³C-CO₂ emitted from chambers that received ¹³C2-pyruvate is primarily formed during decarboxylation in the TCA cycle during energy production (**Fig 1**) (modified from^{25,26}). Using this concept, we can approximate both total (ecosystem-wide flux of) and relative (proportion of total) C allocated to biosynthesis by calculating ¹³C-CO_{2-C1} - ¹³C-CO_{2-C2} (C1 - C2) and ¹³C-CO_{2-C1} / (¹³C-CO_{2-C1} + ¹³C-CO_{2-C2}) (C1/[C2 + C2]), respectively, where ¹³C-CO_{2-C1} and ¹³C2-CO_{2-C2} are efflux from chambers that received ¹³C1-pyruvate or ¹³C1-pyruvate, respectively. To facilitate calculation of Bt and Br, fluxes across time were binned to 0-3 (3 hr), 3 - 6 (6hr), 6 - 12 (12hr), 12 - 18 (18 hr), 18 - 24 (24 hr), 24 - 30 (30 hr), 30 - 36 (36 hr), 36 - 42 (42 hr), and 42 - 48 (48 hr).

3.3.2 VOC data analysis

The isotopic composition of the VOCs flux rate was calculated by applying the linear model to calculate the rate of change in the fractional abundance of ¹³C (¹³C-VOC/[¹³C-VOC + ¹²C-VOC]). For each 6.5 min chamber measurement, a deadband of 30 s was used to allow for mixing in the chamber and the linear model was applied to the successive 10 data points collected at 10 s intervals. VOCs to examine were selected based on two criteria: 1) immediately downstream of pyruvate in the pyruvate metabolism KEGG pathway and 2) VOCs previously detected in soil emissions.

3.3.3 Cumulative fluxes and distribution of ^{13}C from pyruvate

Cumulative ^{13}C - CO_2 and VOC effluxes from 0 to 48 h past ^{13}C -pyruvate injection were calculated using the area under the curve (auc()) function within the flux R package⁷⁰. Based on the total amount of ^{13}C -pyruvate added (100 mg, or 112 mmol), we could determine what percentage of total ^{13}C ended up in CO_2 or VOCs.

3.4 Soil sample collection and processing

For metagenomics, metatranscriptomics, and metabolomics, soil samples were collected just prior to ^{13}C -pyruvate labeling (0 hr) then at 6 and 48 hr post labeling. For 0 hr collection, soil (~ 8 g) was collected directly outside of the stencil using a 2.25 cm diameter sterile metal ring pushed into the soil to 2 cm depth and placed into a sterile 50 mL tube. For 6 and 48 hr collections, soil samples were collected using the same method as for 0 hr, but inside the metal frame where pyruvate labeling occurred. After each soil collection, samples were immediately brought to the lab and allocated for different downstream analyses: 1 g for metabolomics stored at $-20\text{ }^\circ\text{C}$ and 2 g in Lifeguard Soil Preservation Solution (Qiagen) for DNA/RNA extractions stored at $-80\text{ }^\circ\text{C}$.

3.4.1 DNA/RNA extractions

RNA and DNA were co-extracted from 1 g of soil using the RNeasy Powersoil Total RNA Kit (Qiagen) coupled with the RNeasy Powersoil DNA Elution Kit (Qiagen) following the manufacturer's protocol and eluting in 100 μL of kit-provided elution buffer. RNA and DNA quality and concentrations were measured using a Qubit 4 Fluorometer (Thermo Fisher Scientific) and NanoDrop (Thermo Fisher Scientific). RNA was further treated with DNase (DNase Max, Qiagen) to remove any DNA contamination. Total RNA and DNA was sent to the Joint Genome Institute (JGI; Berkeley, CA) for library prep and sequencing.

3.4.2 Water extractions for metabolomics

Water extractions were performed on samples for nuclear magnetic resonance (NMR), followed by solid phase extraction (SPE) for Fourier-transform-ion-cyclotron-resonance MS (FTICR-MS). Water extraction procedures as previously described for bulk metabolite characterization were followed⁷¹⁻⁷³. Briefly, 1 g of soil and 5 mL of double deionized (DDI) water were vortexed in a 15 mL centrifuge tube and sonicated for 2 hours; the sonication bath retained a temperature of $21\text{ }^\circ\text{C}$ to ensure metabolite integrity. The 15 mL centrifuge tube was removed from the sonicator and centrifuged for 20 minutes. One mL of water-extractable organic C (WEOC) was removed and stored at $-80\text{ }^\circ\text{C}$ for NMR analysis at Pacific Northwest National Laboratory (PNNL) while 4 mL of WEOC was saved for downstream SPE.

SPE is an extraction technique used to clean and concentrate samples for the isolation and analysis of organic compounds⁷⁴. Liquid samples are passed through a macroporous styrene-divinylbenzene crosslinked polymer that is able to retain polar organic compounds in water extracted solvents. For this process, Bond Elut PPL (Priority PolLutant) barrel cartridges, which were preactivated with methanol (MeOH), were used. The 4 mL of WEOC were acidified to pH 2 with 1M hydrochloric acid then passed through the sorbent with the vacuum set no higher than -5 pi, to allow compounds to absorb into the retention mechanisms. After the compounds of interest were retained, the cartridges were washed three times with 9 mL of 0.01M hydrochloric acid to remove all impurities. The cartridges were then dried with a pressure air hose for 2-3 minutes and rinsed with 1.5 mL of MeOH in a slow dropwise flow rate into 2 mL vials. The eluate was then capped, stored at -80 °C, and sent to PNNL for FTICR-MS analysis.

3.5 Metabolomics

3.5.1 NMR

¹H-NMR bulk metabolite characterization was performed on soil water extracts. Samples (180 µL) were combined with 2,2-dimethyl-2-silapentane-5-sulfonate-d₆ (DSS-d₆) in D₂O (20 µL, 5 mM) and thoroughly mixed prior to transfer to 3 mm NMR tubes. Resonances corresponding to ¹³C labeling were identified by visual inspection, comparing labeled spectra to unlabeled spectra. Once differences were identified, the molecular location and quantification of ¹³C incorporation was determined by J-coupling pattern analysis and the 'linefitting' tool in Mestrenova, respectively. NMR spectra were acquired on a Bruker Avance III spectrometer operating at a field strength of 17.6 T (¹H ν₀ of 750.24 MHz) and equipped with a 5 mm Bruker TCI/CP HCN (inverse) cryoprobe with Z-gradient and at a regulated temperature of 298 K. The one-dimensional ¹H spectra were acquired using a nuclear Overhauser effect spectroscopy (noesypr1d) pulse sequence. The 90° H pulse was calibrated prior to the measurement of each sample with a spectral width of 12 ppm and 1024 transients. The NOESY mixing time was 100 ms and the acquisition time was 4 s followed by a relaxation delay of 1.5 s during which presaturation of the water signal was applied. Time domain free induction decays (72114 total points) were zero filled to 131072 total points prior to Fourier transform, followed by exponential multiplication (0.3 Hz line-broadening), and semi-automatic multipoint smooth segments baseline correction. Chemical shifts were referenced to the ¹H methyl or ¹³C signal in DSS-d₆ at 0 ppm. The 1D ¹H NMR spectra of all samples were processed, assigned, and analyzed using Chenomx NMR suite 9.2 (Chenomx Inc.; Edmonton, AB, Canada) with quantification of spectral intensities of compounds in the Chenomx library relative to the internal standard. Candidate metabolites present in each of the complex mixtures were determined by matching chemical shift, J-coupling, and intensity information of the experimental signals against signals of the standard metabolites in the Chenomx library. Signal to noise ratios (S/N) were measured using MestReNova v 14.2.014 with the limit of quantification equal to a S/N of 10 and the limit of detection equal to a S/N of 3. Standard 2-D experiments such as ¹H / ¹³C - heteronuclear correlation (HSQC)

experiments or 2-D $^{13}\text{C}/^{13}\text{C}$ Total Correlation spectroscopy (TOCSY) experiments further aided corroboration of several metabolite identifications where there was sufficient S/N.

3.5.2 FTICR

A 12 Tesla Bruker FTICR mass spectrometer (MS) was used to collect high-resolution mass spectra of WEOC by direct injection for secondary metabolite characterization. Approximately 100 μL of water extract was mixed with methanol (1:2) before injection onto the mass spectrometer to enhance ionization. A standard Bruker electrospray ionization (ESI) source was used to generate negatively charged molecular ions. Samples were introduced directly to the ESI source. The instrument settings were optimized by tuning on a Suwannee River fulvic acid standard, purchased from the International Humic Substances Society. Blanks (HPLC grade methanol) were analyzed at the beginning and end of the day to monitor potential carry over from one sample to another. The instrument was flushed between samples using a mixture of water and methanol. The ion accumulation time varied to account for differences in C concentration between samples. One hundred and forty-four individual scans were averaged for each sample and internally calibrated using an OM homologous series separated by 14 Da (CH_2 groups). The mass measurement accuracy was <1 ppm for singly charged ions across a broad m/z range (100–1,000 m/z). The mass resolution was ~ 240 K at 341 m/z . The transient was 0.8 s. Data Analysis software (BrukerDaltonik version 4.2) was used to convert raw spectra to a list of m/z values applying FTICR–MS peak picker module with a signal-to-noise ratio (S/N) threshold set to 7 and absolute intensity threshold to the default value of 100. Putative chemical formulae were then assigned using Formularity software⁷⁵, as previously described⁷⁶. Chemical formulae were assigned based on the following criteria: $\text{S/N} > 7$, mass measurement error <1 ppm, and taking into consideration the presence of C, H, O, N, S, and P and excluding other elements. To ensure consistent formula assignment and eliminate mass shifts that could impact formula assignment, all sample peak lists were aligned to each other. The following rules were implemented to further ensure consistent formula assignment: (a) picking formulae with the lowest error between predicted and observed m/z , and with the lowest number of heteroatoms, and (b) the assignment of one phosphorus atom requires the presence of at least four oxygen atoms. The chemical character of thousands of peaks in each sample's ESI FTICR–MS spectrum was evaluated using van Krevelen diagrams. Biochemical compound classes were reported as relative abundance values based on counts of C, H, and O for the following H:C and O:C ranges: lipids ($0 < \text{O:C} \leq 0.3$ and $1.5 \leq \text{H:C} \leq 2.5$), unsaturated hydrocarbons ($0 \leq \text{O:C} \leq 0.125$ and $0.8 \leq \text{H:C} < 2.5$), proteins ($0.3 < \text{O:C} \leq 0.55$ and $1.5 \leq \text{H:C} \leq 2.3$), amino sugars ($0.55 < \text{O:C} \leq 0.7$ and $1.5 \leq \text{H:C} \leq 2.2$), lignin ($0.125 < \text{O:C} \leq 0.65$ and $0.8 \leq \text{H:C} < 1.5$), tannins ($0.65 < \text{O:C} \leq 1.1$ and $0.8 \leq \text{H:C} < 1.5$), and condensed hydrocarbons (aromatics; $0 \leq 200 \text{ O:C} \leq 0.95$ and $0.2 \leq \text{H:C} < 0.8$)⁷³. Analysis of FTICR data was performed using MetaboDirect (version 0.2.7)⁷⁷ to create profiles of biochemical compound classes, and principal component analysis (PCA) plots.

3.6 Metatranscriptomics and metagenomics

3.6.1 Metagenomics

3.6.1.1 Metagenome libraries

Metagenome libraries were created as previously described⁷⁸ by shearing 100 ng of genomic DNA to 300 bp using the Covaris LE220 instrument and size selected using TotalPure NGS beads (Omega Biotek). The Kapa-HyperPrep kit (Kapa Biosystems) was used to create an unamplified Illumina library, which was paired-end sequenced (2 x 150) on the Illumina NovaSeq 6000 platform using S4 flow cells.

3.6.1.2 Sequence processing

Sequence filtering, assembly, mapping, and annotation were performed at JGI as previously described⁷⁸. Briefly, BBDuk (version 38.94), included in the BBtools package (<https://sourceforge.net/projects/bbmap/>), was used to trim reads that contained adapter sequences, homopolymers of G's of the size 5 or more at the ends of reads, and reads where quality drops to 0. BBDuk was also used to remove reads that contained 1 or more 'N' bases, had an average quality score across the read less than 10, or had a minimum length \leq 51 bp or 33% of the full read length. Reads mapped with BBMap (version 38.44), included in the BBtools package, to masked human, cat, dog, and mouse references at 93% identity common microbial contaminants were removed for downstream analysis. After filtering, each sample had an average of $136,442,170 \pm 36,180,687$ reads and 20.4 ± 5.4 Gb (**Table S2**). Filtered reads were error corrected prior to assembly using bbcms (version 38.90), included in the BBtools package, and assembled using metaSPAdes (version 3.15.2)⁷⁹ with a minimum contig of 200 bp. Filtered reads were then mapped back to contigs using BBMap to obtain coverage information. Each sample had an average of 53.1 ± 6.6 % of filtered reads map to assembled contigs (**Table S2**). Feature prediction was next performed on assembled contigs by using tRNAscan-SE (version 2.0.6) to predict tRNAs, INFERNAL (version 1.1.3)⁸⁰ to identify non-coding (nc) RNAs and rRNAs, CRT-CLI⁸¹ to identify CRISPR regions, and Prodigal (version 2.6.3)⁸² and GeneMarkS-2 (version 1.07)⁸³ to identify protein-coding genes (CDSs). Functional annotation was performed by associating CDSs with Kegg Orthology (KO) terms. Gene copies per KO were calculated as the average coverage of the contigs each gene was predicted from, multiplied by the number of genes in the KO⁷⁸.

3.6.2 Metatranscriptomics

3.6.2.1 Metatranscriptome libraries

rRNA was removed from 10 ng of total RNA using Qiagen FastSelect 5S/16S/23S for bacterial rRNA depletion (and additional FastSelect plant and/or yeast rRNA depletion) (Qiagen) with RNA blocking oligo technology. The fragmented and rRNA-depleted RNA is reverse transcribed to create first strand cDNA using Illumina TruSeq Stranded mRNA Library prep kit (Illumina) followed by the second strand cDNA synthesis which incorporates dUTP to quench the second strand during amplification. The double stranded cDNA fragments are then A-tailed and ligated to JGI dual indexed Y-adapters, followed with an

enrichment of the library by 10 cycles of PCR. Metatranscriptomics of sample P35SSC1_191108_c were not completed due to sequencing issues.

3.6.2.2 Sequence processing

Sequence filtering, assembly, mapping, feature prediction, and annotation were performed by JGI as described above for metagenomics, except for the additional removal of ribosomal RNA during filtering and using MegaHit (version 1.2.9)⁸⁴ for assembly. After filtering, each sample had an average of 91,405,261 ± 35,174,895 reads and 13.0 ± 5.0 Gb, and of these, an average of 73.6 ± 8.3 % mapped to assembled contigs (**Table S2**). Differential expression was performed in DESeq2⁸⁵ on gene copies of KOs, calculated as described above.

3.6.2.3 Weighted gene co-expression network analysis (WGCNA)

WGCNA was performed on metatranscriptomic gene expression data to identify modules of co-expressed genes. First, gene copy data was normalized in DESeq2 using the variance stabilization transformation (VST) method and samples were clustered to detect outliers, which removed only one sample (P15SSC1_191107_c). Next, the normalized data was analyzed using the WGCNA package in R^{86,87}, with the following settings: soft-thresholding power of 6 (chosen based on where scale free topology model fit $R^2 = 0.8$), minimum module size of 80, minimum KME of 0.35, and a 'signed' Topology Overlap Matrix (TOM). Pearson correlation coefficients (r) were calculated between module eigengenes, representing the first component of module, and the following: 1) condition (values for pre-drought and drought set to -1 and 1, respectively) and 2) ¹³C-enrichment of VOCs (acetate-C2 [from C2-¹³C-pyruvate]), acetone-C2, and diacetyl-C2) where values used were the average $^{12}\text{C}/(^{12}\text{C} + ^{13}\text{C})$ flux during a 2 hr window before (48 hr), after (0 hr), or before and after (6 hr +/- 1hr) pyruvate addition.

3.7 VOC cycling genes

Active metabolic pathways were determined by mapping KOs to KEGG pathways using the KEGG pathway mapper tool⁸⁸. VOC cycling genes were chosen based on their being immediately up or downstream from the VOC in the metabolic pathway. Whether the gene was involved in production or consumption of VOC was assessed by whether it was positively or negatively correlated with VOC, respectively, or based on the literature. It should be noted that in some cases, genes can play a role in both the production and consumption of VOC, in which case we relied on the correlation as an indicator.

3.8 Statistical analysis

Statistical analyses of NMR data were performed in R (version 4.0.2). Principal component analysis (PCA) was performed on log-transformed NMR data using `prcomp()` and plotted with `ggplot2`⁸⁹.

The Mann Whitney U-test was used to detect significant differences between pre-drought and drought conditions (data exhibited a non-normal distribution as determined after testing for normality using `ggdensity()`, `ggqqplot()` within the `ggpubr` package (0.4.0), and `shapiro.test()`).

Correlations between ^{13}C -VOCs and gene expression were performed by calculating Spearman correlation coefficients between flux of ^{13}C -enriched VOCs and variance stabilization transformation (VST)-normalized gene copy data. For VOC and CO_2 data, Mann Whitney U-tests were performed between emissions data averaged across all time points between pre-drought and drought conditions. For WGCNA eigengene expression, Kruskal Wallance and Dunn tests were performed to calculate significant differences between pairwise time points post pyruvate addition. All p-values reported (Spearman and Pearson correlations, Mann Whitney U-tests) have been corrected for false discovery rate (FDR) if making multiple comparisons. Enriched KEGG metabolic pathways within each module were calculated using the ClusterProfiler package in R⁹⁰, with the KEGG reference database set to “ko”.

References

1. Schimel, J. P. & Schaeffer, S. M. Microbial control over carbon cycling in soil. *Frontiers in Microbiology* vol. 3 (2012).
2. Insam, H. & Seewald, M. S. A. Volatile organic compounds (VOCs) in soils. *Biol. Fertil. Soils* **46**, 199–213 (2010).
3. Penuelas, J. *et al.* Biogenic volatile emissions from the soil. *Plant Cell Environ.* **37**, 1866–1891 (2014).
4. Honeker, L. K., Graves, K. R., Tfaily, M. M., Krechmer, J. E. & Meredith, L. K. The volatilome: A vital piece of the complete soil metabolome. *Front. Environ. Sci. Eng. China* **9**, (2021).
5. Meredith, L. K. & Tfaily, M. M. Capturing the microbial volatilome: an oft overlooked ‘ome’. *Trends Microbiol.* (2022) doi:10.1016/j.tim.2021.12.004.
6. Koppmann, R. Chemistry of Volatile Organic Compounds in the Atmosphere. *Handbook of Hydrocarbon and Lipid Microbiology* 267–277 (2010) doi:10.1007/978-3-540-77587-4_18.
7. Warren, C. R. Response of osmolytes in soil to drying and rewetting. *Soil Biol. Biochem.* **70**, 22–32 (2014).
8. Schimel, J., Balsler, T. C. & Wallenstein, M. Microbial stress-response physiology and its implications for ecosystem function. *Ecology* **88**, 1386–1394 (2007).
9. Malik, A. A. & Bouskill, N. J. Drought impacts on microbial trait distribution and feedback to soil carbon cycling. *Funct. Ecol.* (2022) doi:10.1111/1365-2435.14010.
10. Vardharajula, S., Department of Microbiology, Agri Biotech Foundation, Acharya N.G. Ranaga Agricultural University, Rajendranagar, Hyderabad,, Andhra Pradesh, India & Sk Z, A. Exopolysaccharide production by drought tolerant *Bacillus* spp. and effect on soil aggregation under drought stress. *J. Microbiol. Biotechnol. Food Sci.* **4**, 51–57 (2014).

11. Sun, S., Lei, H. & Chang, S. X. Drought differentially affects autotrophic and heterotrophic soil respiration rates and their temperature sensitivity. *Biol. Fertil. Soils* **55**, 275–283 (2019).
12. Schimel, J. P. Life in Dry Soils: Effects of Drought on Soil Microbial Communities and Processes. *Annu. Rev. Ecol. Evol. Syst.* (2018) doi:10.1146/annurev-ecolsys-110617-062614.
13. Brown, R. W., Chadwick, D. R., Zang, H. & Jones, D. L. Use of metabolomics to quantify changes in soil microbial function in response to fertiliser nitrogen supply and extreme drought. *Soil Biol. Biochem.* **160**, 108351 (2021).
14. Bouskill, N. J. *et al.* Belowground Response to Drought in a Tropical Forest Soil. I. Changes in Microbial Functional Potential and Metabolism. *Front. Microbiol.* **7**, 525 (2016).
15. Bouskill, N. J. *et al.* Belowground Response to Drought in a Tropical Forest Soil. II. Change in Microbial Function Impacts Carbon Composition. *Front. Microbiol.* **7**, 323 (2016).
16. Fang, H. *et al.* Changes in soil heterotrophic respiration, carbon availability, and microbial function in seven forests along a climate gradient. *Ecol. Res.* **29**, 1077–1086 (2014).
17. Li, Y. *et al.* Effects of biochar application in forest ecosystems on soil properties and greenhouse gas emissions: a review. *J. Soils Sediments* **18**, 546–563 (2018).
18. Su, X. *et al.* Drought changed soil organic carbon composition and bacterial carbon metabolizing patterns in a subtropical evergreen forest. *Sci. Total Environ.* **736**, 139568 (2020).
19. Peñuelas, J. & Llusà, J. BVOCs: plant defense against climate warming? *Trends Plant Sci.* **8**, 105–109 (2003).
20. Bourtsoukidis, E. *et al.* Strong sesquiterpene emissions from Amazonian soils. *Nat. Commun.* **9**, 2226 (2018).
21. Jardine, K. *et al.* Dimethyl sulfide in the Amazon rain forest. *Global Biogeochem. Cycles* **29**, 19–32 (2015).
22. Reichstein, M. *et al.* Climate extremes and the carbon cycle. *Nature* **500**, 287–295 (2013).
23. Jentsch, A. & Beierkuhnlein, C. Research frontiers in climate change: Effects of extreme meteorological events on ecosystems. *C. R. Geosci.* **340**, 621–628 (2008).
24. Bore, E. K., Apostel, C., Halicki, S., Kuzyakov, Y. & Dippold, M. A. Soil microorganisms can overcome respiration inhibition by coupling intra- and extracellular metabolism: ¹³C metabolic tracing reveals the mechanisms. *The ISME Journal* vol. 11 1423–1433 (2017).
25. Dijkstra, P. *et al.* Modeling soil metabolic processes using isotopologue pairs of position-specific ¹³C-labeled glucose and pyruvate. *Soil Biol. Biochem.* **43**, 1848–1857 (2011).
26. Dijkstra, P. *et al.* Probing carbon flux patterns through soil microbial metabolic networks using parallel position-specific tracer labeling. *Soil Biology and Biochemistry* vol. 43 126–132 (2011).
27. Albright, M. B. N. *et al.* Differences in substrate use linked to divergent carbon flow during litter decomposition. *FEMS Microbiol. Ecol.* **96**, (2020).
28. Drake, H. L., Küsel, K. & Matthies, C. Ecological consequences of the phylogenetic and physiological diversities of acetogens. *Antonie Van Leeuwenhoek* **81**, 203–213 (2002).

29. Williams, F. R., Robert Williams, F. & Hager, L. P. Crystalline flavin pyruvate oxidase from *Escherichia coli*. *Archives of Biochemistry and Biophysics* vol. 116 168–176 (1966).
30. Schreiner, M. E. & Eikmanns, B. J. Pyruvate:quinone oxidoreductase from *Corynebacterium glutamicum*: purification and biochemical characterization. *J. Bacteriol.* **187**, 862–871 (2005).
31. Carter, K. & Gennis, R. B. Reconstitution of the Ubiquinone-dependent pyruvate oxidase system of *Escherichia coli* with the cytochrome *o* terminal oxidase complex. *J. Biol. Chem.* **260**, 10986–10990 (1985).
32. Khandokar, Y. B., Londhe, A., Patil, S. & Forwood, J. K. Expression, purification and crystallization of acetyl-CoA hydrolase from *Neisseria meningitidis*. *Acta Crystallogr. Sect. F Struct. Biol. Cryst. Commun.* **69**, 1303–1306 (2013).
33. Buu, L.-M., Chen, Y.-C. & Lee, F.-J. S. Functional Characterization and Localization of Acetyl-CoA Hydrolase, Ach1p, in *Saccharomyces cerevisiae*. *Journal of Biological Chemistry* vol. 278 17203–17209 (2003).
34. Fleck, C. B. & Brock, M. Re-characterisation of *Saccharomyces cerevisiae* Ach1p: fungal CoA-transferases are involved in acetic acid detoxification. *Fungal Genet. Biol.* **46**, 473–485 (2009).
35. Chen, Y., Zhang, Y., Siewers, V. & Nielsen, J. Ach1 is involved in shuttling mitochondrial acetyl units for cytosolic C2 provision in *Saccharomyces cerevisiae* lacking pyruvate decarboxylase. *FEMS Yeast Res.* **15**, (2015).
36. Carman, A. J., Vylkova, S. & Lorenz, M. C. Role of acetyl coenzyme A synthesis and breakdown in alternative carbon source utilization in *Candida albicans*. *Eukaryot. Cell* **7**, 1733–1741 (2008).
37. Shi, L. & Tu, B. P. Acetyl-CoA and the regulation of metabolism: mechanisms and consequences. *Curr. Opin. Cell Biol.* **33**, 125–131 (2015).
38. Ince, B. *et al.* Inhibition effect of isopropanol on acetyl-CoA synthetase expression level of acetoclastic methanogen, *Methanosaeta concilii*. *J. Biotechnol.* **156**, 95–99 (2011).
39. Awang, G. M., Jones, G. A. & Ingledew, W. M. The acetone-butanol-ethanol fermentation. *Crit. Rev. Microbiol.* **15 Suppl 1**, S33–67 (1988).
40. Maddox, I. S. The acetone-butanol-ethanol fermentation: recent progress in technology. *Biotechnol. Genet. Eng. Rev.* **7**, 189–220 (1989).
41. Karl, T., Striednig, M., Graus, M., Hammerle, A. & Wohlfahrt, G. Urban flux measurements reveal a large pool of oxygenated volatile organic compound emissions. *Proc. Natl. Acad. Sci. U. S. A.* **115**, 1186–1191 (2018).
42. Kosar, F., Akram, N. A., Sadiq, M., Al-Qurainy, F. & Ashraf, M. Trehalose: A Key Organic Osmolyte Effectively Involved in Plant Abiotic Stress Tolerance. *Journal of Plant Growth Regulation* vol. 38 606–618 (2019).
43. Kakumanu, M. L., Ma, L. & Williams, M. A. Drought-induced soil microbial amino acid and polysaccharide change and their implications for C-N cycles in a climate change world. *Sci. Rep.* **9**, 10968 (2019).

44. Werner, C. *et al.* Ecosystem fluxes during drought and recovery in an experimental forest. *Science* **374**, 1514–1518 (2021).
45. Honeker, L. K. *et al.* Elucidating Drought-Tolerance Mechanisms in Plant Roots through ¹H NMR Metabolomics in Parallel with MALDI-MS, and NanoSIMS Imaging Techniques. *Environ. Sci. Technol.* **56**, 2021–2032 (2022).
46. Schmidt, O., Hink, L., Horn, M. A. & Drake, H. L. Peat: home to novel syntrophic species that feed acetate- and hydrogen-scavenging methanogens. *The ISME Journal* vol. 10 1954–1966 (2016).
47. Kempf, B. & Bremer, E. Uptake and synthesis of compatible solutes as microbial stress responses to high-osmolality environments. *Arch. Microbiol.* **170**, 319–330 (1998).
48. Trchounian, A. A. A direct interaction between the H⁺-F₁F₀-ATPase and the K⁺ transport within the membrane of anaerobically grown bacteria. *Bioelectrochemistry and Bioenergetics* vol. 33 1–10 (1994).
49. Abdel-Hamid, A. M., Attwood, M. M. & Guest, J. R. Pyruvate oxidase contributes to the aerobic growth efficiency of *Escherichia coli*. *Microbiology* **147**, 1483–1498 (2001).
50. Wolfe, A. J. The acetate switch. *Microbiol. Mol. Biol. Rev.* **69**, 12–50 (2005).
51. Barnard, R. L., Osborne, C. A. & Firestone, M. K. Responses of soil bacterial and fungal communities to extreme desiccation and rewetting. *ISME J.* **7**, 2229–2241 (2013).
52. Waring, B. G. & Hawkes, C. V. Short-term precipitation exclusion alters microbial responses to soil moisture in a wet tropical forest. *Microb. Ecol.* **69**, 843–854 (2015).
53. Sun, Y. *et al.* Drought stress induced increase of fungi:bacteria ratio in a poplar plantation. *CATENA* vol. 193 104607 (2020).
54. Börjesson, T., Stöllman, U. & Schnürer, J. Volatile metabolites produced by six fungal species compared with other indicators of fungal growth on cereal grains. *Appl. Environ. Microbiol.* **58**, 2599–2605 (1992).
55. Zhao, D. F. *et al.* Environmental conditions regulate the impact of plants on cloud formation. *Nat. Commun.* **8**, 14067 (2017).
56. McBride, S. G., Osburn, E. D., Barrett, J. E. & Strickland, M. S. Volatile methanol and acetone additions increase labile soil carbon and inhibit nitrification. *Biogeochemistry* **145**, 127–140 (2019).
57. Boulton, C. A., Lenton, T. M. & Boers, N. Pronounced loss of Amazon rainforest resilience since the early 2000s. *Nat. Clim. Chang.* **12**, 271–278 (2022).
58. Pegoraro, E., Rey, A., Abrell, L., Haren, J. & Lin, G. Drought effect on isoprene production and consumption in Biosphere 2 tropical rainforest. *Glob. Chang. Biol.* **12**, 456–469 (2006).
59. van Haren, J. L. M. *et al.* Drought-induced nitrous oxide flux dynamics in an enclosed tropical forest. *Glob. Chang. Biol.* **11**, 1247–1257 (2005).
60. Pegoraro, E. *et al.* Effect of elevated CO₂ concentration and vapour pressure deficit on isoprene emission from leaves of *Populus deltoides* during drought. *Funct. Plant Biol.* **31**, 1137–1147 (2004).

61. Leigh, L. S., Burgess, T., Marino, B. D. V. & Wei, Y. D. Tropical rainforest biome of Biosphere 2: Structure, composition and results of the first 2 years of operation. *Ecol. Eng.* **13**, 65–93 (1999).
62. Fasbender, L., Yáñez-Serrano, A. M., Kreuzwieser, J., Dubbert, D. & Werner, C. Real-time carbon allocation into biogenic volatile organic compounds (BVOCs) and respiratory carbon dioxide (CO₂) traced by PTR-TOF-MS, ¹³C₂O laser spectroscopy and ¹³C-pyruvate labelling. *PLoS One* **13**, e0204398 (2018).
63. Holzinger. PTRwid: A new widget tool for processing PTR-TOF-MS data. *Atmospheric Measurement Techniques*.
64. de Gouw, J. *et al.* Sensitivity and specificity of atmospheric trace gas detection by proton-transfer-reaction mass spectrometry. *Int. J. Mass Spectrom.* **223–224**, 365–382 (2003).
65. Holzinger, Acton & Bloss. Validity and limitations of simple reaction kinetics to calculate concentrations of organic compounds from ion counts in PTR-MS. *Measurement*.
66. de Gouw, J. & Warneke, C. Measurements of volatile organic compounds in the earth's atmosphere using proton-transfer-reaction mass spectrometry. *Mass Spectrom. Rev.* **26**, 223–257 (2007).
67. Krechmer, J. *et al.* Evaluation of a New Vocus Reagent-Ion Source and Focusing Ion-Molecule Reactor for use in Proton-Transfer-Reaction Mass Spectrometry. doi:10.26434/chemrxiv.6502652.
68. Clafin, M. S. *et al.* An in situ gas chromatograph with automatic detector switching between PTR- and EI-TOF-MS: isomer-resolved measurements of indoor air. *Atmospheric Measurement Techniques* vol. 14 133–152 (2021).
69. Gil-Loaiza, J. *et al.* Versatile soil gas concentration and isotope monitoring: optimization and integration of novel soil gas probes with online trace gas detection. *Biogeosciences* vol. 19 165–185 (2022).
70. Koebisch, F., Glatzel, S. & Jurasinski, G. Vegetation controls methane emissions in a coastal brackish fen. *Wetlands Ecol. Manage.* **21**, 323–337 (2013).
71. Tfaily, M. M. *et al.* Advanced solvent based methods for molecular characterization of soil organic matter by high-resolution mass spectrometry. *Anal. Chem.* **87**, 5206–5215 (2015).
72. Tfaily, M. M. *et al.* Single-throughput Complementary High-resolution Analytical Techniques for Characterizing Complex Natural Organic Matter Mixtures. *J. Vis. Exp.* (2019) doi:10.3791/59035.
73. Tfaily, M. M. *et al.* Sequential extraction protocol for organic matter from soils and sediments using high resolution mass spectrometry. *Anal. Chim. Acta* **972**, 54–61 (2017).
74. Dittmar, T., Koch, B., Hertkorn, N. & Kattner, G. A simple and efficient method for the solid-phase extraction of dissolved organic matter (SPE-DOM) from seawater. *Limnology and Oceanography: Methods* vol. 6 230–235 (2008).
75. Tolić, N. *et al.* Formularity: software for automated formula assignment of natural and other organic matter from ultrahigh-resolution mass spectra. *Anal. Chem.* **89**, 12659–12665 (2017).
76. Tfaily, M. M. *et al.* Vertical Stratification of Peat Pore Water Dissolved Organic Matter Composition in a Peat Bog in Northern Minnesota. *Journal of Geophysical Research: Biogeosciences* **123**, 479–494

- (2018).
77. Ayala-Ortiz, C. O. *et al.* MetaboDirect: An Analytical Pipeline for the processing of FTICR-MS-based Metabolomics Data. doi:10.1101/2022.06.10.495699.
 78. Clum, A. *et al.* DOE JGI Metagenome Workflow. *mSystems* **6**, (2021).
 79. Nurk, S., Meleshko, D., Korobeynikov, A. & Pevzner, P. A. metaSPAdes: a new versatile metagenomic assembler. *Genome Res.* **27**, 824–834 (2017).
 80. Nawrocki, E. P. & Eddy, S. R. Infernal 1.1: 100-fold faster RNA homology searches. *Bioinformatics* **29**, 2933–2935 (2013).
 81. Bland, C. *et al.* CRISPR recognition tool (CRT): a tool for automatic detection of clustered regularly interspaced palindromic repeats. *BMC Bioinformatics* **8**, 209 (2007).
 82. Hyatt, D. *et al.* Prodigal: prokaryotic gene recognition and translation initiation site identification. *BMC Bioinformatics* **11**, 119 (2010).
 83. Lomsadze, Tang, Gemayel & Borodovsky. GeneMarkS-2: Raising Standards of Accuracy in Gene Recognition. *exon.gatech.edu*.
 84. Li, D., Liu, C.-M., Luo, R., Sadakane, K. & Lam, T.-W. MEGAHIT: an ultra-fast single-node solution for large and complex metagenomics assembly via succinct de Bruijn graph. *Bioinformatics* **31**, 1674–1676 (2015).
 85. Love, M. I., Huber, W. & Anders, S. Moderated estimation of fold change and dispersion for RNA-seq data with DESeq2. *Genome Biol.* **15**, 550 (2014).
 86. Langfelder, P. & Horvath, S. WGCNA: an R package for weighted correlation network analysis. *BMC Bioinformatics* vol. 9 (2008).
 87. Langfelder, P. & Horvath, S. FastRFunctions for Robust Correlations and Hierarchical Clustering. *Journal of Statistical Software* vol. 46 (2012).
 88. Kanehisa, M. & Sato, Y. KEGG Mapper for inferring cellular functions from protein sequences. *Protein Science* vol. 29 28–35 (2020).
 89. Wilkinson, L. ggplot2: Elegant Graphics for Data Analysis by WICKHAM, H. *Biometrics* vol. 67 678–679 (2011).
 90. Wu, T. *et al.* clusterProfiler 4.0: A universal enrichment tool for interpreting omics data. *Innovation (N Y)* **2**, 100141 (2021).

Declarations

Acknowledgements

A portion of this research was performed under the Facilities Integrating Collaborations for User Science (FICUS) exploratory effort and used resources at the US Department of Energy (DOE) Joint Genome Institute (proposal ID 1292415) and the Environmental Molecular Sciences Laboratory (proposal ID 50971 - award DOI: 10.46936/fics.proj.2019.50971/60000130), which are DOE Office of Science User

Facilities. This research was supported, in part, by the European Research Council (ERC; Grant Number 647008) and the Department of Energy, Office of Science Biological and Environmental Research Grant (DE-SC0021349). L.H. was supported by Biosphere 2 through the office of the Senior Vice President for Research Innovation and Impact at the University of Arizona. G. P. was supported by the German Federal Ministry of Education and Research (BMBF contract 01LB1001A – ATTO+) and the Max Planck Society. The authors gratefully acknowledge financial support from the Phileology Foundation.

Figures

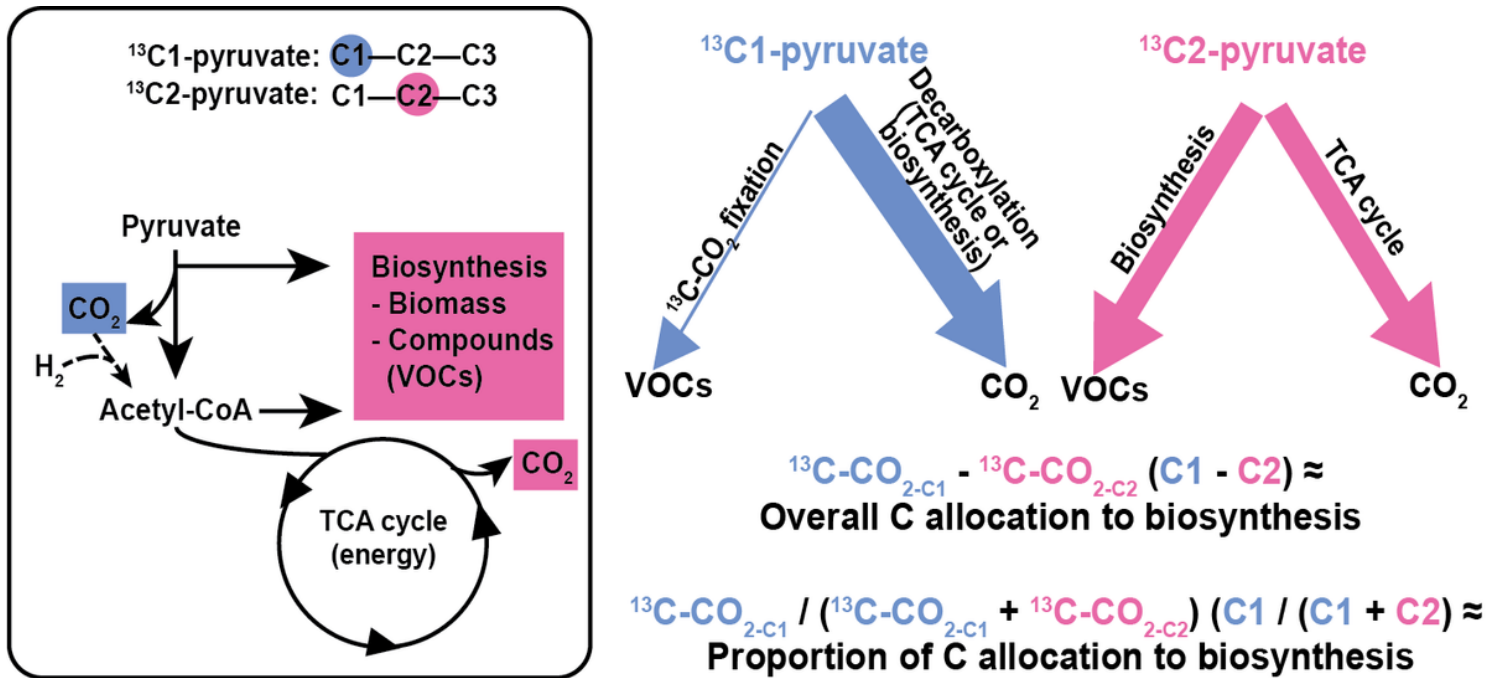


Figure 1

Framework depicting how 1st (C1; blue) and 2nd (C2; pink) carbon (C) positions of pyruvate from ¹³C1-pyruvate and ¹³C2-pyruvate, respectively, is expected to be allocated into CO₂ and biosynthetic (including VOCs) pathways. As indicated by the thickness of the arrows, we expect most C1 to be released as CO₂ during biosynthesis and TCA cycle, and C2 to be either released as CO₂ in the TCA cycle or used for biosynthesis of biomass and products. The difference in ¹³C-CO_{2-C1} - ¹³C-CO_{2-C2} approximates the overall ecosystem-wide C allocation to biosynthesis, while the ratio ¹³C-CO_{2-C1} / (¹³C-CO_{2-C1} + ¹³C-CO_{2-C2}) approximates the proportion of internal C allocation to biosynthesis.

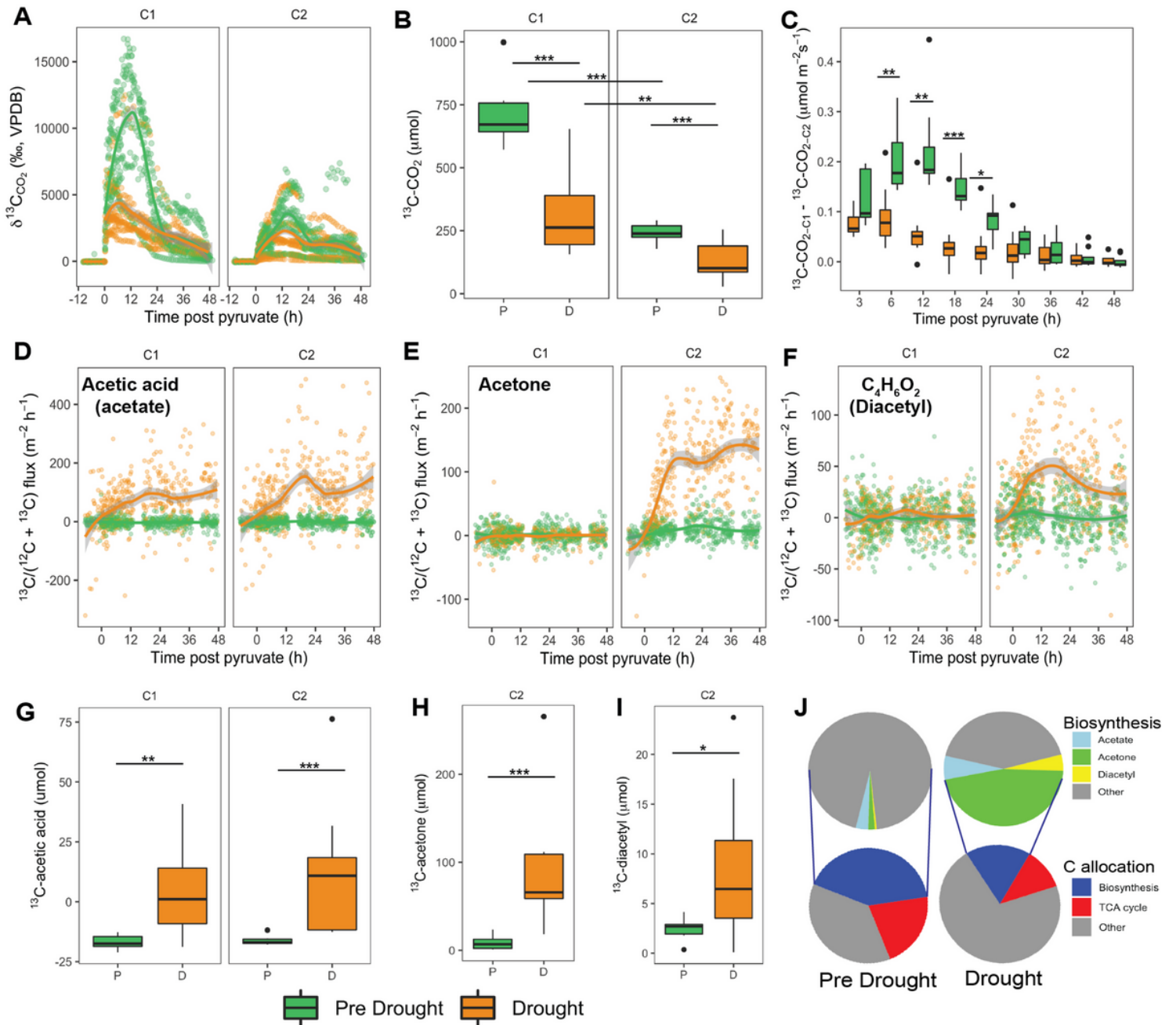


Figure 2

Drought induces a shift in C allocation, as measured using position-specific ^{13}C -pyruvate labeling. A) Drought induces decrease in $\delta^{13}\text{C}$ value of the CO_2 efflux over time from 12 h pre- to 48 h post-pyruvate injection from both $^{13}\text{C1}$ -pyruvate and $^{13}\text{C2}$ -pyruvate. B) Drought induces a decrease in cumulative $^{13}\text{C}\text{-CO}_2$ soil efflux (μmol) from 0 to 48 h post-pyruvate injection. C) Overall C allocation to biosynthesis (calculated as C1 - C2 of $^{13}\text{C}\text{-CO}_2$), with significant increases during pre-drought from 3 - 24 h post ^{13}C -pyruvate injection. Continuous emission data was binned to 3 or 6 h intervals. Flux of ^{13}C -enriched D) acetic acid, E) acetone, and F) $\text{C}_4\text{H}_6\text{O}_2$ from 0 to 48 h post pyruvate injection were higher during drought, with acetone and $\text{C}_4\text{H}_6\text{O}_2$ peaking after ~12 h and acetic acid peaking after ~18 h following pyruvate

injection, with acetone peaking a second time at ~36 h. Cumulative flux of G) ^{13}C -acetic acid increased during drought compared to pre-drought conditions for chambers receiving both $^{13}\text{C}1$ - and $^{13}\text{C}2$ -pyruvate. Cumulative flux of H) ^{13}C -acetone and I) ^{13}C - $\text{C}_4\text{H}_6\text{O}_2$ increased during drought compared to pre-drought conditions. J) Bottom pie charts show the percentage of ^{13}C from pyruvate allocated to biosynthesis or TCA cycle (or other which could represent un-metabolized pyruvate or uncharacterized pathways) for pre-drought (left) and drought (right). Of the ^{13}C allocated to biosynthesis, top pie charts show the percentage allocated to the VOCs acetic acid, acetone, and diacetyl (or other which could include different compounds or biomass). For all time series (A, C, D - F), each point represents a single sample measurement and includes 3 replicates each of C1 and C2- ^{13}C -pyruvate per 3 sites (total $n = 18$) for pre-drought and drought conditions. For all box plots (B, G, H, I), the box represents Q1 - Q3 of all sites and time points with the center line indicating the median, and whiskers extending to the minimum and maximum values exclusive of outliers (separate black points) ($n = 54$ each for pre-drought and drought). P, pre-drought; D, drought; *, $p < 0.05$; **, $p < 0.01$; ***, $p < 0.001$

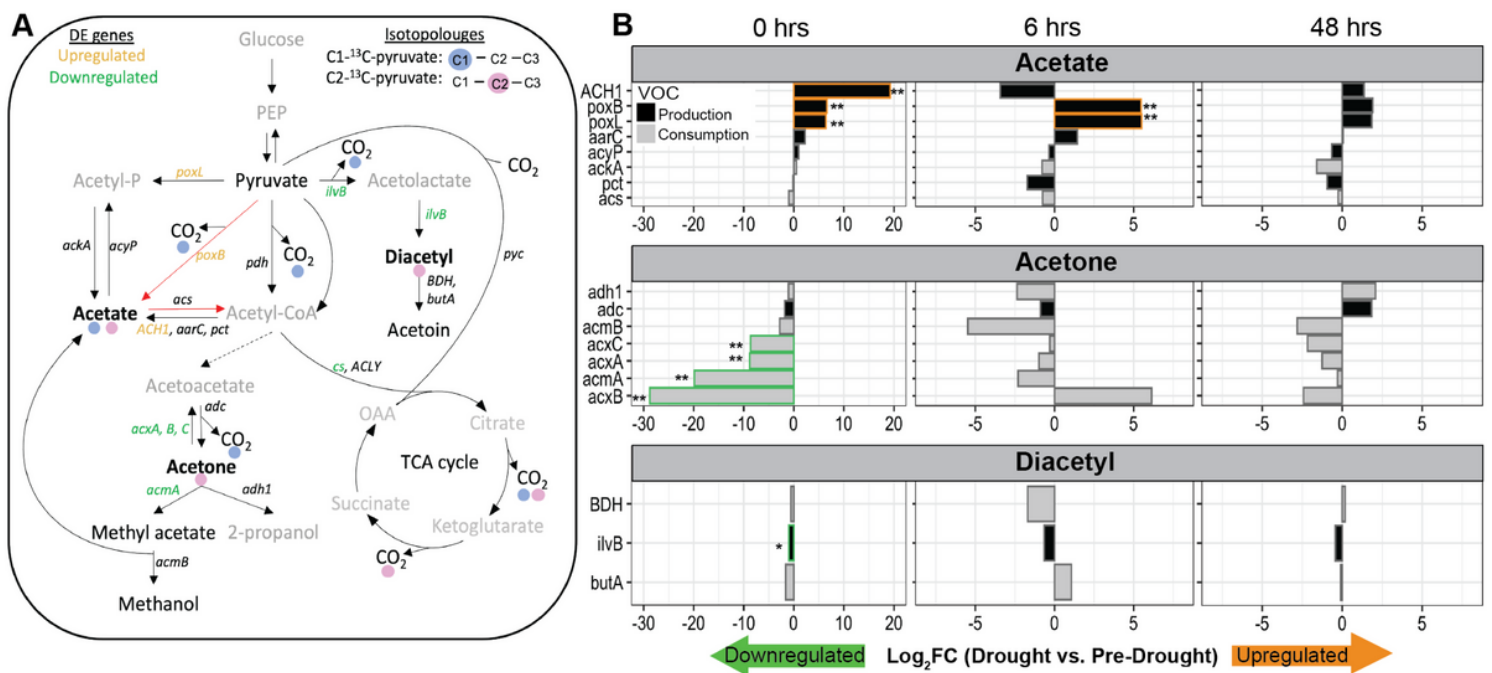


Figure 3

Expression of genes encoding for enzymes that cycle ^{13}C -enriched VOCs shifts with drought. A) Pyruvate metabolism pathways that lead to ^{13}C -enriched VOCs and CO_2 , shown with blue and pink circles, to represent incorporation of ^{13}C -pyruvate from the C1 and/or C2 position, respectively. Gray names indicate the compound was not detected. Bold names are the ^{13}C -enriched VOC compounds (acetate, acetone, diacetyl). Arrows indicate the direction of reactions labeled with genes for enzymes catalyzing each reaction. Red arrows represent a potential PDH bypass route of acetyl-CoA production from pyruvate to acetate to acetyl-CoA. Green and orange gene names signify down- or upregulation during drought, respectively, compared to pre-drought conditions. B) Changes in gene expression across all sites (for pre-

drought, 0 and 48 h [n = 6], 6 h [n = 5]); for drought (n = 6 for each time point) as log₂ fold-change (log₂FC) during drought compared to pre-drought for acetate, acetone, and diacetyl (C₄H₆O₂) at 0, 6, and 48 hours post pyruvate addition. Genes that encode for enzymes involved in production are in black, and consumption in gray. *, p < 0.05; **, p < 0.001 (Deseq2); *poxB*, pyruvate-dehydrogenase quinone; *poxL*, pyruvate oxidase; *ACH1*, acetyl-CoA hydrolase; *aarC*, acetate CoA-transferase; *ackA*, acetate kinase; *acyP*, acylphosphatase; *acs*, acetyl-CoA synthetase; *pct*, propionate CoA-transferase; *adh1*, alcohol dehydrogenase; *acm*, acetone monooxygenase; *acxA-C*, acetone carboxylase; *adc*, acetoacetate decarboxylase; *BDH/butA*, butanediol dehydrogenase/ diacetyl reductase; *ilvM*, acetolactate synthase; *cs*, citrate synthase; OAA, oxaloacetate; PEP, phosphoenolpyruvate

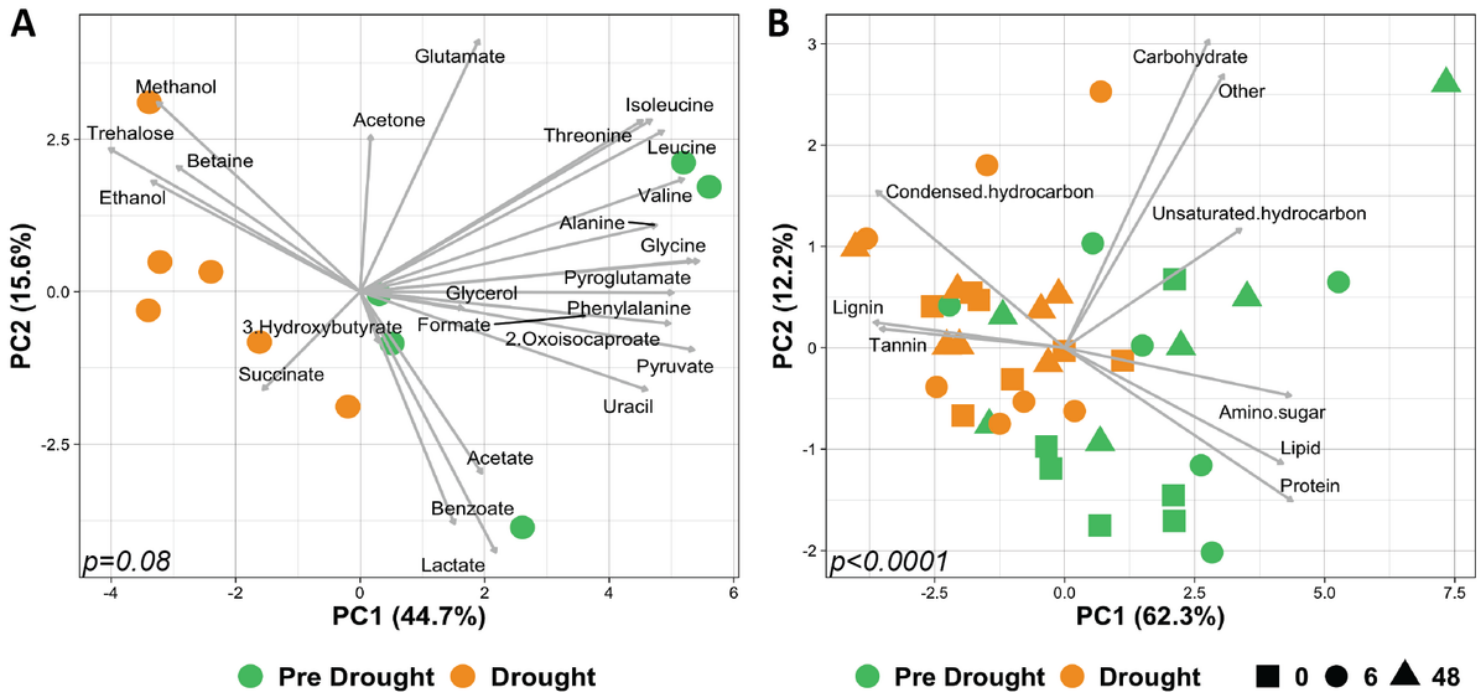


Figure 4

Drought induced a shift in both primary and secondary metabolic composition. A) PCA biplot of samples collected during pre-drought (green; 0 h [n = 5]) or drought (orange; 0 h [n = 5] and 6 h [n = 1]) showing relationships between metabolic profiles identified with NMR which were mostly identified as primary metabolites with relatively low molecular weight. Arrows represent the loadings of individual metabolites. B) PCA biplot of samples collected during pre-drought (green) or drought (orange) showing relationships between profiles of metabolic classes identified with FTICR-MS, capturing mostly high molecular weight metabolites including secondary metabolites. Arrows represent the loadings of metabolic classes driving these patterns. P-values indicate significance of clustering between pre-drought and drought conditions using PERMANOVA on bray-curtis dissimilarity matrix.

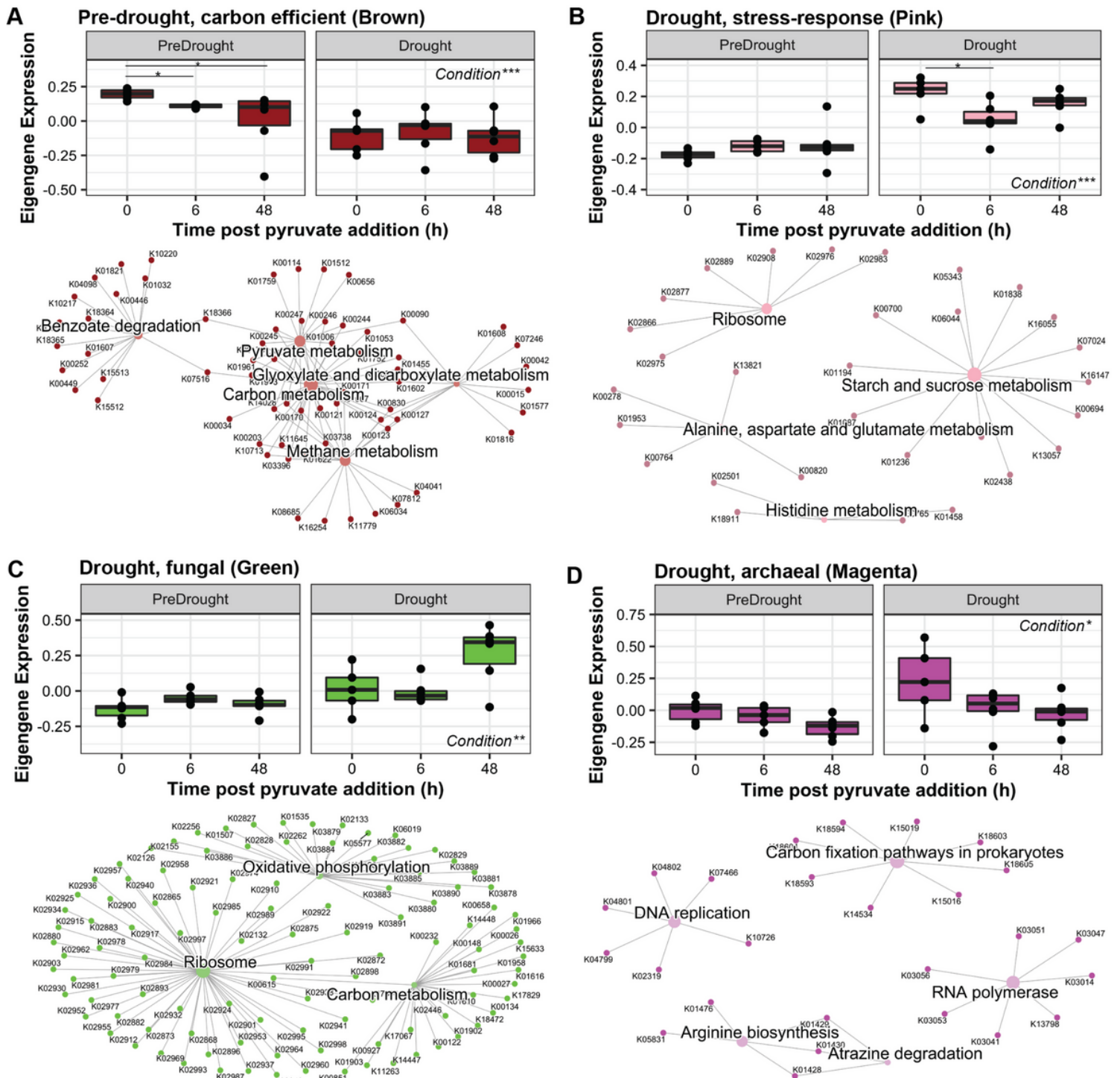


Figure 5

Expression of pre-drought and drought-associated gene modules and their networks of enriched KEGG metabolic pathways. The top portion of each panel shows eigengene expression at 0, 6, and 48 hrs post pyruvate addition during pre-drought (0 and 48 h [n = 6], 6 h [n = 5]) and drought (6 and 48 h [n = 6], 0 h [n = 5]) conditions for the subset of modules - A) brown, B) pink, C) green, and D) magenta. Expression values are arbitrary units. Each point represents one sample, with bars representing Q1 - Q3 with center line indication median, and bars extending to maximum and minimum values, excluding outliers. The bottom of each panel shows a metabolic network of enriched KEGG pathways within the module. Central nodes

represent the pathway and each branch represents the KO group within that pathway. *, $p < 0.05$; **, $p < 0.01$; ***, $p < 0.001$ (Mann-Whitney for condition, Kruskal-Wallis for pairwise comparisons between time-points)

Supplementary Files

This is a list of supplementary files associated with this preprint. Click to download.

- [Supplemental.docx](#)